Research Article

ADVANCED PHOTONICS

Temperature-adaptive metasurface radiative cooling device with excellent emittance and low solar absorptance for dynamic thermal regulation

Junlin Yang, Qianyi Li, Shiqiao Liu, Debao Fang, Jingyao Zhang, Haibo Jin,* and Jingbo Li*

Beijing Institute of Technology, School of Materials Science and Engineering, Beijing Key Laboratory of Construction Tailorable Advanced Functional Materials and Green Applications, Beijing, China

Abstract. Passive radiative cooling is a promising passive cooling technology that emits heat to deep space without energy consumption. Nevertheless, the persistent challenge of overcooling in static radiative techniques has raised concerns. Although a desirable solution is suggested based on vanadium dioxide (VO_2) in the form of a Fabry–Perot (F–P) resonant cavity, the inherent contradiction between desired high emissivity (ε) and low solar absorptance (α_{sol}) remains a notable limitation. Here, we employed a simple mask-filling technique to develop a temperature-adaptive metasurface radiative cooling device (ATMRD) for dynamic thermal regulation. Simulation and experimental results substantially evidenced that multiple localized polariton resonances were induced by the VO_2 metasurface, significantly enhancing the thermal emittance of the ATMRDs. The engineered ATMRD achieved an amazing switch of the atmospheric window emittance from 0.13 to 0.85 when the surface temperature exceeds a pre-set transition temperature, accompanied by a commendable α_{sol} of 27.71%. The mechanism of multiple localized polariton resonances is discussed in detail to understand the enhanced performance based on the investigation of the relationship between the metasurface structure and multiple localized polariton resonances. We demonstrate an efficient smart radiative technique achieved by a simple micro/nanoprocess and, most importantly, contribute a valuable reference for the design of radiative devices, which is crucial in various areas such as passive cooling, smart windows, multifunctional electromagnetic response, and space application technologies.

Keywords: dynamic radiative cooling; metasurface; vanadium dioxide; emittance; plasmon resonance.

Received Mar. 10, 2024; revised manuscript received Jul. 1, 2024; accepted for publication Aug. 7, 2024; published online Aug. 30, 2024; corrected Sep. 3, 2024.

[DOI: 10.1117/1.AP.6.4.046006]

1 Introduction

The demand for green and sustainable energy-saving technologies has extensively promoted the development of refrigeration technology. Radiative cooling is emerging as a cutting-edge technology, attracting widespread attention for its unique working principle.[1–7] Compared with other refrigeration technologies,[8–11] radiative cooling can efficiently reduce the object's temperature without external power sources or refrigerants, eliminating the limitations of traditional refrigeration methods and achieving more flexible and efficient energy utilization.

Passive radiative cooling relies on the emission of heat from terrestrial objects to the 3K outer space through the thermal infrared transparency window (~8 to 14 μm), commonly referred to as the "atmospheric window." To effectively dissipate heat, materials for passive radiative cooling are typically designed with minimal solar absorptance (α_{sol}) in the wavelength range of 0.3 to 2.5 μm and maximal thermal emittance (ε) within the atmospheric window. Such a property has been realized in various materials such as herbs,[1,12] paints,[13–15] fabrics,[16–18] and ceramics.[7,19] However, the emissivity of these schemes remains static and is usually designed for daytime radiative cooling, which will cause unnecessary overcooling due to continuous heat dissipation when the object's temperature is lower than desired. Very recently, emittance-adaptive devices have

*Address all correspondence to Jingbo Li, lijb@bit.edu.cn; Haibo Jin, hbjin@bit.edu.cn

been developed to achieve dynamic thermal regulation. A promising solution is employing thermochromic phase-change materials to switch automatically between radiative cooling and heat-retaining modes, effectively addressing the well-known overcooling problem of daytime passive radiative cooling.[3,5,20,21] Typically, a vanadium dioxide (VO_2) radiative cooling system in the form of a Fabry–Perot (F–P) resonant cavity achieves self-switching in thermal radiation, providing a promising design for dynamic radiative cooling.[22,23] However, the inherent contradiction between desired high emissivity and low solar absorptance remains a notable limitation in such radiative devices. The emittance and solar absorptance are sensitively dependent on the structure of the devices and the thickness of VO_2.[24] Usually, achieving a high emittance comes at the expense of solar absorptance and vice versa, leading to limited upgradability. Recently, it has been demonstrated that patterned micro–nano-structures with subwavelength dimensions for the VO_2 surface induce plasmonic resonances, effectively boosting the absorption of electromagnetic waves.[25–28] Some preliminary designs have also proposed to overcome the mutual constraints of VO_2-based F–P resonator radiative devices.[29–32] Although this solution is highly desirable, existing efforts are either purely theoretical simulations or are limited by fabrication technology due to too small or complex micro–nano-structures requiring high-precision etching technology. In addition, the relationship between the size of micro–nano-structure and performance (e.g., α_{sol} and ε) has not yet been comprehensively evaluated and verified by experiment.

In this work, we designed and prepared a temperature-adaptive metasurface radiative cooling device (ATMRD). The ATMRD is a simple sandwich structure consisting of silver (Ag), hafnium oxide (HfO_2), and patterned VO_2. Through optical simulation and experimental verification, the size range of the optimal VO_2 micro-structure that achieves synergy between solar absorptance and emittance was clarified. Based on the results of simulation optimization, the ATMRD with the best VO_2 microstructure was fabricated using sample mask-filling engineering. The prepared ATMRD exhibited excellent radiative cooling and solar reflectivity performance, automatically switching the atmospheric window ε from 0.13 to 0.85 when the surface temperature exceeds a pre-set transition temperature; meanwhile, achieving a satisfactory α_{sol} of 27.71% at 20°C (or 35.44% at 90°C). The potential applications were further evaluated using simulated solar heating tests and infrared (IR) thermography. This scheme represents a significant advancement in balancing conflicting requirements to enhance radiative cooling performance. Simultaneously, the adoption of a simple and cost-effective micro–nano-preparation technology offers a practical solution for the fabrication of micro-nanostructures.

2 Results

2.1 Design of Radiative Cooling Device and Numerical Modeling

Figure 1(a) illustrates a typical temperature-adaptive radiative device (ATRD) based on the F–P resonator. A highly reflective metal layer is placed at the bottom, followed by a middle layer of highly IR transparent material and a continuous VO_2 film covers the top. In the insulating (I) state of VO_2 at $T < T_{MIT}$ (metal–insulator transition temperature), VO_2 allows high transmission of IR light, and incident IR light is reflected by the bottom metal layer, achieving a low IR absorption. The heat inside the object cannot radiate away, preventing the overcooling phenomenon. By contrast, the ATRD becomes highly absorptant to IR light when VO_2 switches to the metal (M) state at $T > T_{MIT}$. The absorption is further amplified in the atmospheric window through a design of a 1/4 wavelength cavity.[3] According to Kirchhoff's law, the IR absorptance (A) equals emittance (ε) for IR opaque materials.[33] Hence, the emittance achieves a temperature-adaptive switch in the atmospheric window from low to high (or high to low) depending on the I–M phase transition of VO_2, as illustrated in Fig. 1(b).

Here, the reflective layer uses an Ag metal with the highest reflection compared with other common metals [Figs. S1(a) and S1(b) in the Supplementary Material], which will contribute to achieving a high solar reflection [Fig. S1(c) in the Supplementary Material]. HfO_2 is selected as the dielectric layer due to its high IR transparency at a broad bandwidth.[34] The simulated optimal emittance tunability ($\Delta\varepsilon = 0.66$) can be achieved in ATRD by optimizing the thickness of the HfO_2 and VO_2 layer (Fig. S2 in the Supplementary Material), whereas the α_{sol} is 33.48% at low temperature [the dotted horizontal line in Fig. 2(h)] and 43.51% at high temperature [the dotted horizontal line in Fig. 2(i)]. High solar absorptance, especially at high temperatures, will cause the object's temperature to increase and weaken the radiation heat dissipation ability to a certain extent during daytime.

Aiming at the goal of achieving low α_{sol} and high ε, we employ a periodic array pattern to replace the continuous VO_2 film, as depicted in Figs. 1(c) and 1(d), namely, constructing an ATMRD. The incorporation of VO_2 metasurface can obviously reduce α_{sol} and enhance ε through rational structural design to tune the resonant frequency to the atmospheric window, as shown in Figs. 1(e) and 1(f). The resonant frequency of the metasurface strongly depends on the structure parameters of the top metallic patterns,[35] including geometric shape, arrangement period (P), feature size (L), and gap (G) with the relation $P = L + G$, as shown in Fig. 1(c). We create simple squares and circular patterns to consider the effects of L and G on α_{sol} and ε. For convenience, the samples with different L and G for squares and circular patterns are labeled as Lx-Gy and Dx-Gy, respectively, where x represents the variation of L or D from 1 to 10 μm, and y represents the G ranging from 0.5 to 3 μm. The simulated solar absorptance results for ATMRD with a square array structure are presented in Figs. 2(a) and 2(b) and Fig. S3 in the Supplementary Material. The amplitude of the solar absorptance curve for all samples gradually weakens as G increases at a fixed L or L decreases at fixed G. The same trend is found in ATMRD with a circular array structure shown in Fig. S4 in the Supplementary Material, indicating that α_{sol} significantly depends on the coverage area of VO_2 in ATMRD. The integration results in Figs. 2(c) and 2(d) using Eq. (1) (see Sec. 4.2) suggest a proportional relationship between α_{sol} and the coverage area of VO_2: the larger the VO_2 coverage area, the stronger α_{sol}.

Figures 3(a)–3(g) show the simulated emissivity spectra of ATMRD with the square patterns of different L and G in the frequency range from 2.5 to 20 μm. Compared with the emissivity spectra of ATRD, additional peaks are induced by the periodic VO_2 patterns besides the $1/4n\lambda$ resonant absorption peak. Variations in feature size L and gap G significantly impact the intensity and position of the emittance peak as VO_2 is in the metallic phase. When L is fixed, both the emissivity intensity and bandwidth increase as G becomes narrower. As L increases

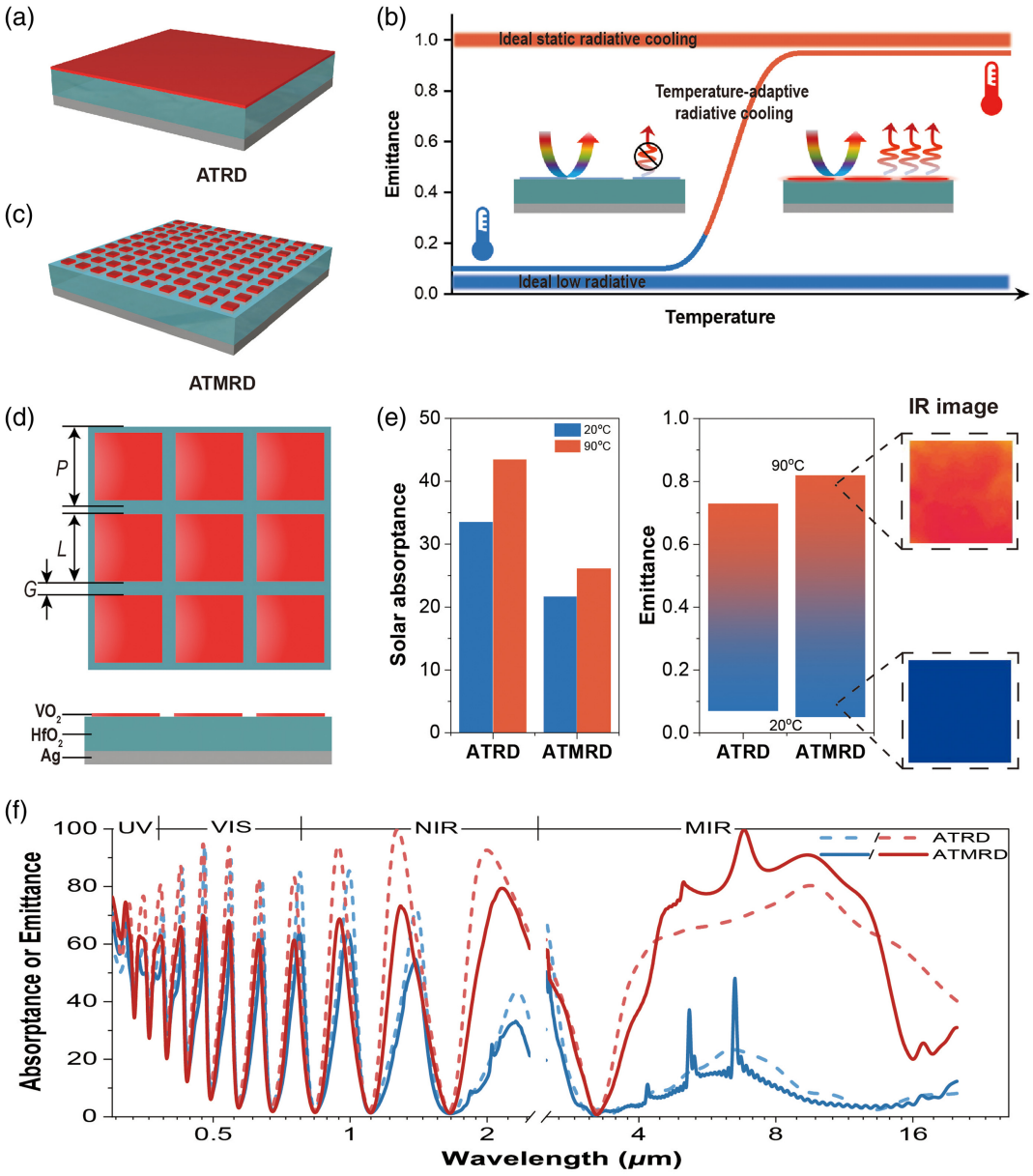

Fig. 1 (a), (c) Schematics of the ATRD and the ATMRD. (b) Working diagram of the ideal temperature-adaptive radiative cooling. (d) Surface pattern dimensions and cross-sectional diagram of designed ATMRD. (e), (f) Comparison of simulated solar absorptance and thermal emissivity between ATRD and ATMRD. The blue line represents low temperature, and the red line represents high temperature.

at fixed G, the intensity of the enhanced emissivity peak gradually decreases, whereas the long wave absorption edge shifts toward a longer wavelength, as shown in Fig. 3(g). A comparison is carried out for different L or G in the same period P ($P = L + G$), as shown in Fig. S5 in the Supplementary Material. It is found that the emissivity intensity and bandwidth obviously increase as L increases, or G decreases at fixed P when VO_2 is in the metallic phase. The thermal emittances (ε) at different L and G are calculated with Eq. (2) (presented in Sec. 4.2) by referencing the blackbody radiation spectra and exhibited in Fig. 3(h). At low temperatures, the thermal emittance (ε_L) of ATMRD is lower than that of ATRD, which is more beneficial in preventing the overcooling of objects at low temperatures. As the feature size L increases in ATMRD, the ε_L slightly increases due to the increased area of VO_2. In comparison, the emittance at high temperature (ε_H) is significantly enhanced. The ε_H of ATMRD increases rapidly with increasing L as $L \leq 4$ and reaches the maximum value at $L = 4$ for the G0.5 and G1 ATMRDs, followed by a slight decline with a further increase in L. As $L \geq 4$, the ε_H of G1 and G0.5 surpasses that of ATRD. However, the ε_H of ATMRD with a larger gap ($G > 1$) is lower than that of ATRD. The emittance tunability ($\Delta\varepsilon$) of ATMRD outperforms ATRD over a broader pattern range when $L > 2$ and $G \leq 1$, with the peak value located at $L = 4$, as shown in Fig. 3(i). The results of ATMRD with a circular array structure (Fig. S6 in the Supplementary Material)

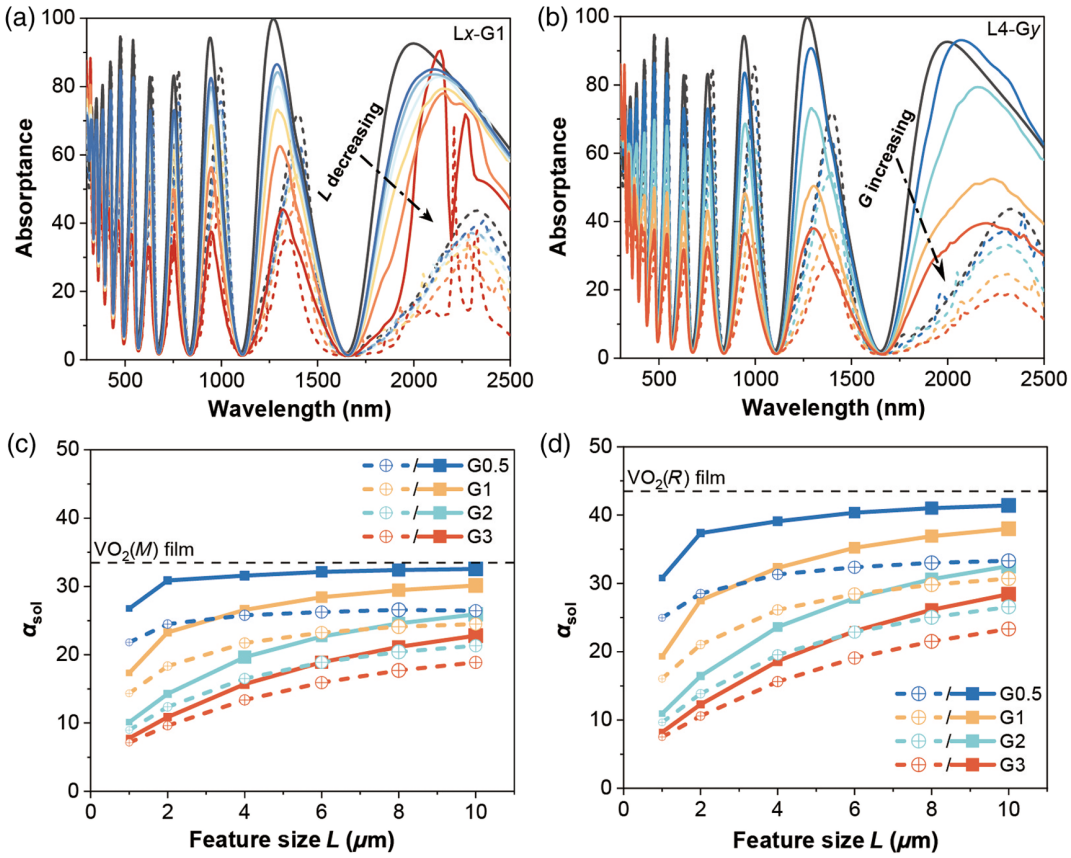

Fig. 2 (a), (b) Simulated solar absorptance spectra for ATMRD Lx-Gy samples with $x = 1, 2, 4, 6, 8$, and 10 μm and $y = 0.5$, 1, 2, and 3 μm. Here, the dotted and solid lines represent the I and M states of VO_2, respectively. The dark line represents the solar absorptance spectra of ATRD. The simulated solar absorptance as a function of feature size L along with gap size G at temperatures of (c) 25°C and (d) 90°C. Note that signed solid lines and dashed lines represent simulation results for square and circular patterns, respectively. The size of the symbol indicates the variation of the feature size.

also revealed consistent regularity, with slightly lower $\Delta\varepsilon$ than square patterns [Fig. 3(i)] because the rounded corners of circular patterns increase the gap G. The above results indicate that the appropriate values of feature size and gap (or period) are crucial to achieving emittance enhancement.

2.2 Preparation and Characterization of ATMRD

Based on the above simulated results, we selected three representative feature sizes ($L = 4$, 6, and 8 μm) and three gap values ($G = 1$, 2, and 3 μm) to fabricate ATMRD using a simple mask-filling engineering. The experimental section describes the fabrication process in detail. Figure 4(a) exhibits a photograph of the ATMRD. It presents a rainbow spectrum under visible light due to the structural color induced by the micro–nanostructure.[36] The cross-sectional scanning electron microscopy (SEM) image and energy dispersive spectroscopy (EDS) mapping of the ATMRD in Fig. 4(b) exhibit good adhesion among different layers, providing a fundamental guarantee for the device's performance. The thickness of the Ag, HfO_2, and VO_2 layers is 100, 800, and 50 nm, respectively. Figure 4(c) shows the SEM morphology of the ATMRD's top view. All samples present well-designed geometries over the range of feature sizes L from 4 to 8 μm and G from 1 to 3 μm, attributed to advanced photolithography and magnetron sputtering deposition technology. This method can significantly reduce manufacturing costs and achieve scale preparation compared with electron beam lithography.

Figures 5(a) and 5(b) show the X-ray diffractometer (XRD) and Raman results of ATMRD films for phase identification. The XRD pattern in Fig. 5(a) primarily exhibits the crystalline structure of HfO_2, along with diffraction peaks of Ag. No other impurities are observed. The Raman results in Fig. 5(b) confirm the existence of the M1-phase VO_2 film.[37] In addition, the VO_2 film reveals an excellent IR switch from high transmittance and high reflectance at $T_{MIT} = 68$°C, as shown in Figs. 5(c) and 5(d).

2.3 Radiative Cooling Performance of ATMRD

The emissivity spectra of ATMRD are detected under different temperatures, as depicted in Figs. 6(a)–6(d). The emissivity of the devices changes significantly from low to high values with the increase in temperature. The ATRD exhibits strong absorption for wavelengths larger than 4 μm, with an emissivity peak at ~8 μm when heated to 90°C [Fig. 6(a)], corresponding to the blackbody radiation peak. For ATMRD at 90°C, the peak

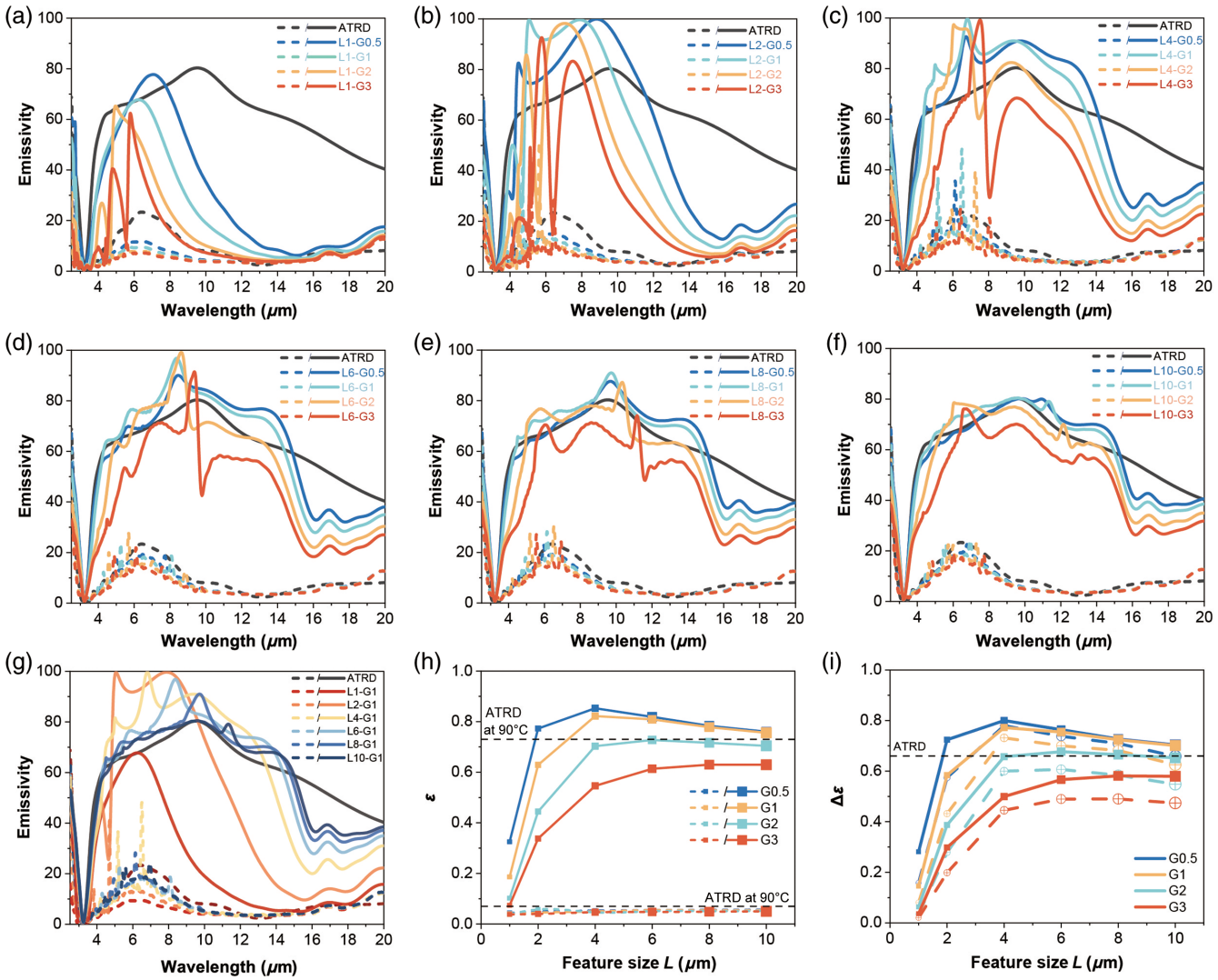

Fig. 3 (a)–(g) Simulated emissivity spectra at different L and G for ATMRD with square array structure. (h) ε value and (i) $\Delta\varepsilon$ as a function of L at different G. Note that the dotted and solid lines in panels (a)–(g) represent the insulator and metal states of VO_2, respectively. The solid lines and dashed lines in panel (i) represent the simulation results for square and circular patterns, respectively.

intensity of L4-G1 and L6-G1 devices is significantly enhanced and almost reaches 100% [Figs. 6(b) and 6(c)], whereas L8-G1 shows a slight decrease in peak intensity [Fig. 6(d)]. The increasing L causes the peak to shift toward longer wavelengths, as indicated in Figs. 6(b)–6(d) and Fig. 7(a). The temperature-dependent thermal emittances are obtained from Figs. 6(a)–6(d) using Eq. (2), intuitively evaluating the $\Delta\varepsilon$, as shown in Figs. 6(e)–6(h). A rapid switch from ε_L to ε_H is observed when the temperature exceeds T_{MIT}. The ε_H values for L4-G1, L6-G1, and L8-G1 are 0.85, 0.89, and 0.84, respectively, representing a more than 13% improvement over ATRD's value of 0.75. As the temperature gradually declines, the ε_H can maintain over a broad temperature range and then switch to ε_L at ~50°C due to a typical hysteresis effect of VO_2 phase transition, contributing to more effective heat dissipation at high temperatures. However, the thermal emissivity gradually decreases as G broadens from 1 to 3 μm at a fixed L, as shown in Fig. S7 in the Supplementary Material. Only Lx-G1 achieves significantly improved emittance compared with ATRD, as indicated in Fig. 7(b), which is consistent with the simulated results. The $\Delta\varepsilon$ of ATMRD-L4-G1 ($\Delta\varepsilon = 0.72$) is enhanced by 20% compared with the ATRD ($\Delta\varepsilon = 0.6$).

Figures 6(i)–6(m) and Fig. S8 in the Supplementary Material present the measured solar absorptance spectra at low and high temperatures. The relationship of solar absorptance, feature size, and gap size at 20°C and 90°C is illustrated in Fig. 7(c), respectively. Solar absorptance at low temperatures shows a noticeable decline in ATMRD compared with ATRD (35.25%). When ATMRD switches to the ε_H state, solar absorptance rises slightly but remains significantly lower than ATRD's (46.55%). Solar absorptance of the L4-G1 is 27.71% at low temperatures and rises to 35.44% at high temperatures. ATMRDs with more significant gaps achieve smaller solar absorptance but lower emissivity. Hence, the ATMRD L4-G1 achieves optimal performance with $\alpha_{\mathrm{sol}} = 27.71\%$ at 20°C ($\alpha_{\mathrm{sol}} = 35.44\%$ at 90°C) and $\varepsilon_H = 0.85$ ($\Delta\varepsilon = 0.72$), as shown in Fig. 7(d).

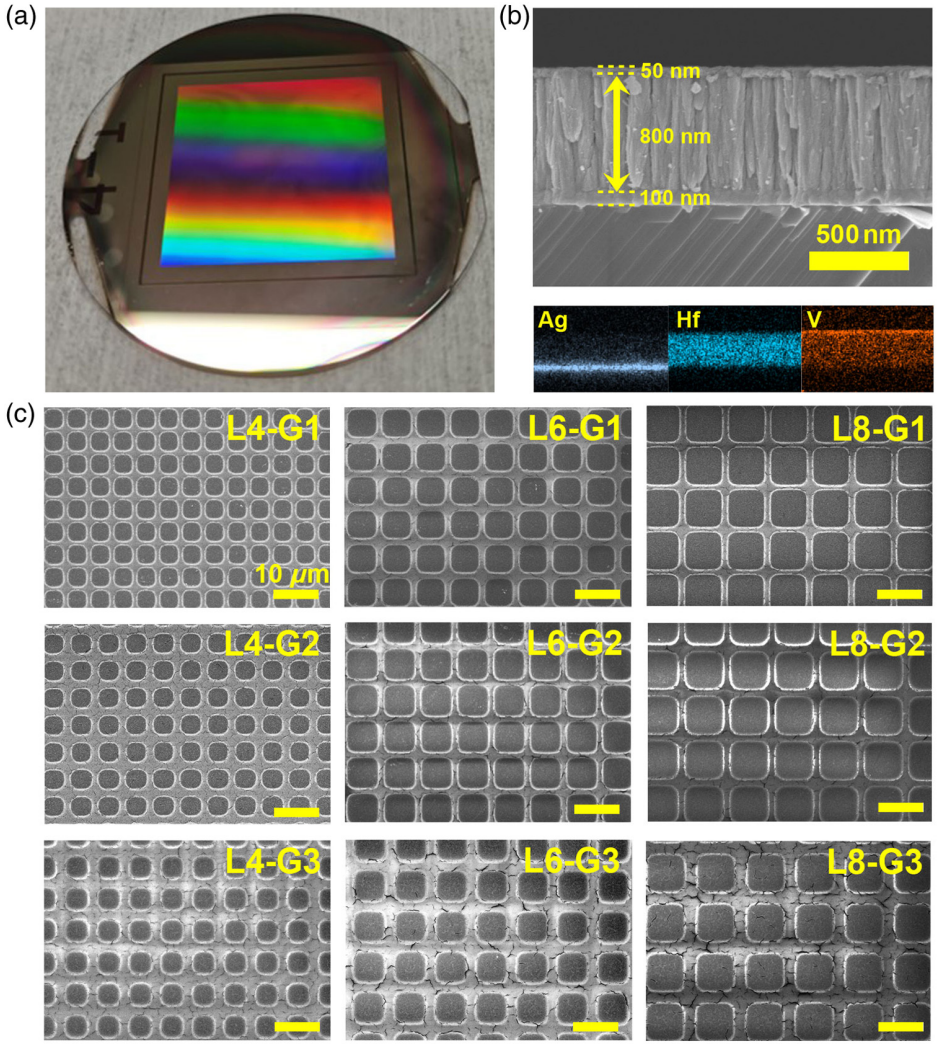

Fig. 4 (a) Photograph of ATMRD L4-G1, and the middle colored area is the micro–nanostructure. (b) Cross-sectional SEM image and EDS mappings of ATMRD. (c) SEM morphology of the ATMRD's top view with different *L* and *G*.

Figure 7(e) compares the emittance performance of dynamic radiation cooling devices reported in recent years. The performance of the radiative cooling device designed in this work is better than most literature results, affirming the viability of the design scheme and preparation method presented in this study.

2.4 Application Potential Assessment

We carried out verification experiments to evaluate the practical application potential of ATMRD devices. A solar simulator was employed to conduct a preliminary test of the sunlight reflection capability; the schematic diagram is shown in Fig. 8(a). The 3M tape ($\varepsilon = 0.96$), silicon (Si) wafer ($\varepsilon = 0.5$), and aluminum (Al) sheet ($\varepsilon = 0.1$) are selected as reference samples. The results in Fig. 8(b) show that the temperature of ATRD quickly rises and then gradually levels off to 37°C within 120 s, but the temperature is much lower than that of the 3M tape (53°C) and Si wafer (44°C). The ATMRD presents a lower temperature than the ATRD, and the temperature further declines toward that of the Al sheet with decreasing *L*. The temperature of ATMRD L4-G1 is only 33°C, slightly higher than that of the Al sheet (28°C). Such a low solar absorptance significantly reduces solar radiation interference to the cooling device.

The emittance switching of ATMRD, along with two reference samples, was examined by IR imaging with a thermal IR camera, as shown in Fig. 8(c). One reference sample is an Al sheet, which features a consistently low thermal emittance of 0.10, and the other is the commercial 3M tape, possessing a steady high thermal emittance of 0.96, pasted over the Al_2O_3 substrate used in ATMRD. Compared with the two references, the ATMRD shows a significant thermal radiation change over the VO_2 phase transition [Fig. 8(d)]. Before the phase transition, the thermal radiation of ATMRD is consistent with that of the Al sheet and then switches to a high emittance state after the phase transition. Moreover, the emittance exhibits weak dependence on the detection angle, as displayed in Fig. 8(e). The result demonstrates that the ATMRD has excellent solar reflectance and considerable heat dissipation.

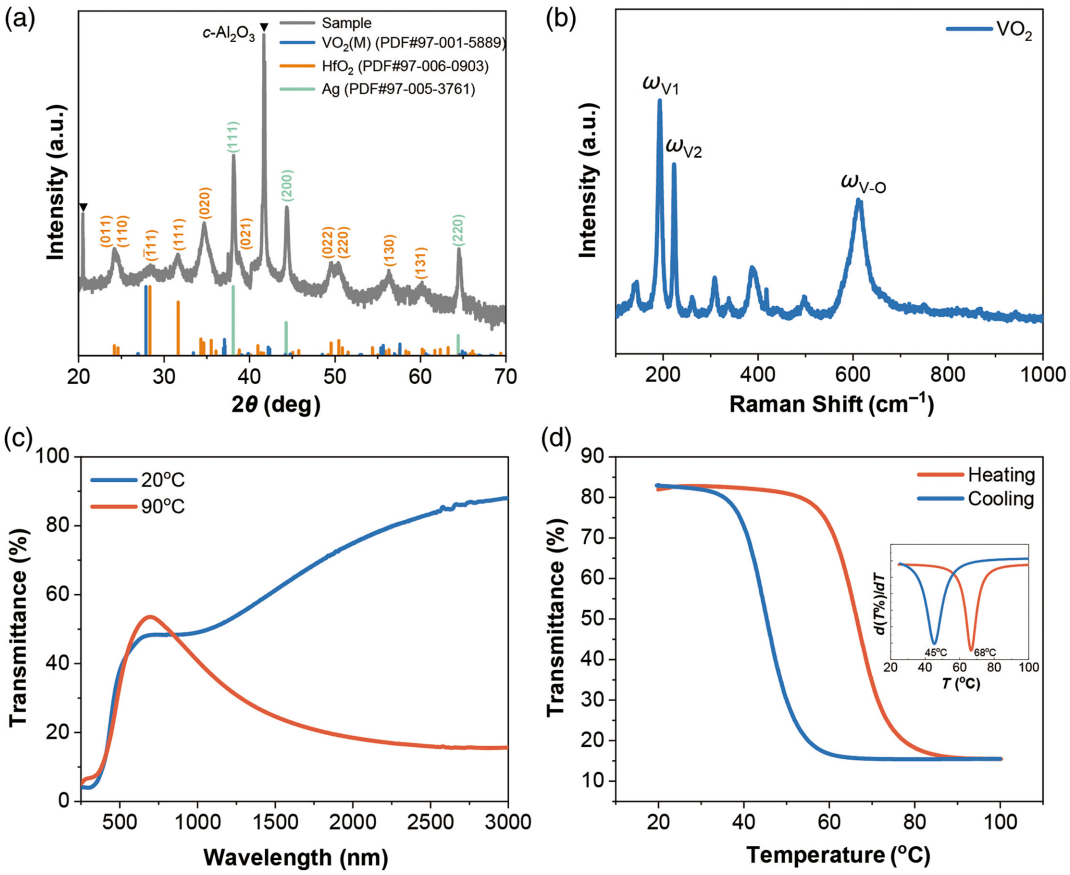

Fig. 5 (a) XRD pattern of the ATMRD. (b) Raman spectrum at room temperature for VO_2 films. (c) UV-VIS-NIR transmittance spectra at 20°C and 90°C of VO_2 film deposited on a sapphire substrate for reference. (d) Temperature-dependent transmittance of the VO_2 film at a wavelength of 2500 nm. The inset shows the corresponding $d(T\%)/dT - T$ curves in the heating cycle using Lorentz function fitting.

2.5 Mechanism Analysis

To elucidate the underlying mechanism responsible for the metasurface-enhanced absorption based on the F–P resonant cavity, electromagnetic field distributions in the x–z cross section of one array cell [Fig. 9(a)] were investigated for ATMRDs with different feature size L with VO_2 in the metal phase. Coupled with the F–P resonances in ATRD [Fig. 9(c)], the multimode polariton resonances are excited in ATMRD, as shown in Figs. 9(d)–9(k) and Figs. S9–S11 in the Supplementary Material, producing the corresponding sharp peaks in the emissivity spectra in Fig. 3. The results show that the polariton resonance strongly depends on the structural parameters of feature size and gap size or period of the metasurface.

The surface plasmon polariton (SPP) resonance emerges on the surface of the VO_2 units when the feature size L (or period P) matches the wavelength of the incident wave. For ATMRD L4-G1, the SPP resonance occurs at ~5 μm due to the strong electric polarization above the VO_2 units in Fig. 9(d). For L6-G1, L8-G1, and L10-G1, the SPP resonance appears at 7, 9, and 11 μm, respectively, as shown in Figs. S10C and S11E in the Supplementary Material and Fig. 9(k).

As the incident wavelength $\lambda > P$, the electric polarization in the HfO_2 medium between the metallic VO_2 and the Ag substrate gradually increases, as characterized by the polarized electric field vectors, which indicate electric current loops in Figs. 9(e)–9(g). The alternatively polarized electric field induces strong localized magnetic polaritons (MPs).[47] The electromagnetic polariton resonances can be understood by employing an equivalent inductor–capacitor (LC) circuit model.[48] The sandwiched HfO_2 spacer serves as a capacitor (C), whereas the top metallic VO_2 microstructure and the bottom Ag substrate function as inductors ($L_k + L_m$), as illustrated in Fig. 9(b), forming a resonant LC circuit. The LC circuit induces the magnetic field and develops magnetic dipoles according to Lenz's law.[49] Eventually, the localized strong magnetic field is induced at the resonance frequency of the magnetic and electric dipoles, where the total impedance equals zero.[35] In other words, the MP resonance is excited at the resonance frequency, resulting in an enhanced absorption effect. At 6.8 μm, an intense MP resonance centers below the gaps of VO_2 units of L4-G1 in Fig. 9(e). As the wavelength of incident light becomes longer, the induced electric polarization period also changes for a longer period of time. The strong polariton resonances occur at ~9.2 and ~12.5 μm, with the enhanced magnetic response centering below the VO_2 units, as shown in Figs. 9(f) and 9(g). Further increasing the incident wavelength, the polarization becomes weak. Hence, the emissivity spectrum experiences gradual suppression at a longer wavelength.

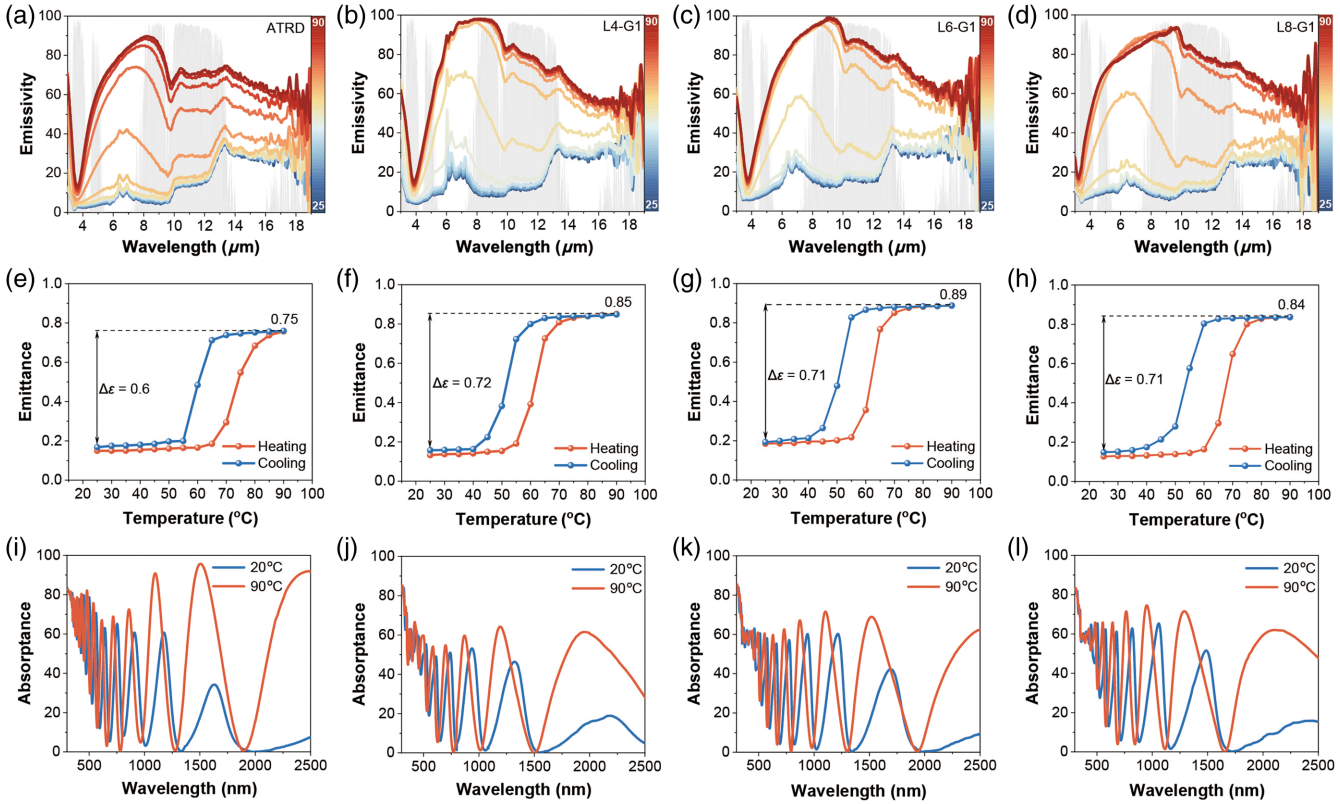

Fig. 6 Thermal emissivity spectra at different temperatures, emittance-dependent temperature during heating and cooling, and solar absorptance at low and high temperatures for (a), (e), (i) ATRD, (b), (f), (j) ATMRD L4-G1, (c), (g), (k) ATMRD L6-G1, and (d), (h), (l) ATMRD L8-G1, respectively.

For $\lambda < P$, the polarized electric field period is smaller than the feature size L. Figures 9(i) and 9(j) indicate two localized SPP resonances on one VO_2 unit for L8-G1 and L10-G1. This is because two periodic polarization electric fields are formed on the surface of each metallic VO_2 unit when λ is half of P, thus exciting two localized SPP resonances. Meanwhile, the multiple MP resonances can also be excited between VO_2 layers and Ag layers at resonant frequencies. However, the polarization strength gradually weakens as the λ becomes much smaller than P. Therefore, the metastructure loses its effects, as λ is much smaller than P.

3 Discussion

We have successfully designed and fabricated the temperature-adaptive metasurface radiative device—ATMRD by sample mask-filling engineering. The fabrication of a VO_2 metasurface resolves the issue of balancing high emittance and low solar absorptance. The metasurface stimulates the localized polariton resonances as VO_2 in the metallic state, enhancing the absorption of electromagnetic radiation in the thermal IR and declining α_{sol} through reducing the area of VO_2. The fabricated ATMRD L4-G1 demonstrates the ability to switch the atmospheric window thermal emittance from 0.13 to 0.85 over the VO_2 phase transition. Meanwhile, it achieves a commendable α_{sol} of 27.71%. The simulation-based analysis reveals the relationship between the structural parameters of the metasurface and performance, providing a guide for the design of metasurface radiative cooling devices. The solar absorptance is directly proportional to the coverage area of VO_2, independent of the pattern shape. However, in terms of emissivity, the structural parameters (feature size and gap size or period) of the metasurface play a pivotal role in triggering the polariton resonances of different manners at specific frequencies. Reduced pattern gaps facilitate the enhancement of IR absorption, whereas the feature sizes of 4 and 6 μm perform the optimal thermal emittance because they can ultimately excite the polariton resonances in the thermal IR range.

4 Appendix: Materials and Methods

4.1 Fabrication of Radiative Cooling Device

Radiative cooling devices featuring a triple-layer film structure of $Ag/HfO_2/VO_2$ were fabricated on a c-Al_2O_3 substrate using magnetron sputtering. Initially, a reflective layer of Ag was deposited on the substrate using a high-purity Ag target. Subsequently, an 800-nm HfO_2 layer was deposited utilizing a ceramic target. For ATRD, a 50-nm-thick layer of vanadium is directly deposited on the top of the HfO_2 layer using a high-purity metal vanadium target at room temperature. The vanadium film underwent thermal treatment to transform into the VO_2 M1 phase using a rapid annealing furnace (RTP-500, Beijing East-star Research Office of Applied Physics, Beijing, China). For ATMRD, the VO_2 microstructure was fabricated through mask-filling engineering, as illustrated in Fig. S12 in the Supplementary Material.

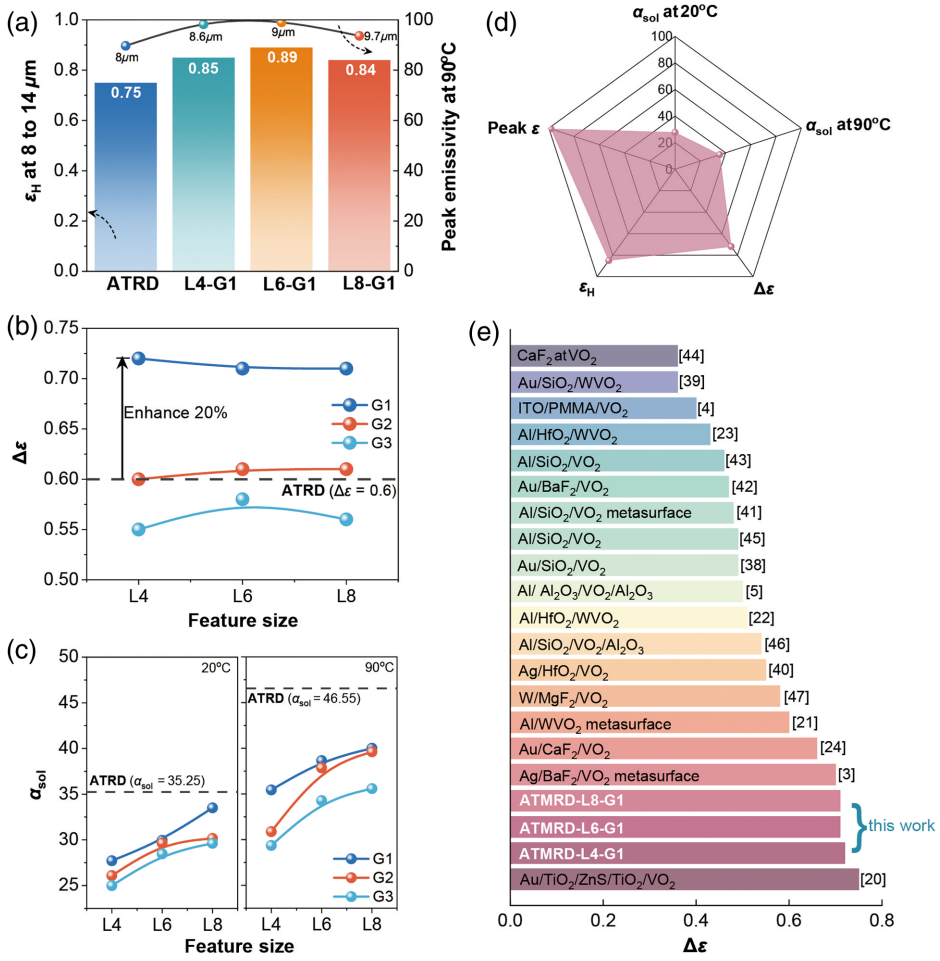

Fig. 7 (a) Comparison of the thermal emittance. (b) Comparison of emittance tunability between ATMRD L*x*-G*y* and ATRD. (c) Comparison of solar absorptance between ATMRD L*x*-G*y* and ATRD at different temperatures. (d) Optimal performance of ATMRD L4-G1. (e) Comparison of the emittance performance with previous reports.[3–5,20–24,38–48]

The pre-prepared Ag/HfO_2 device underwent plasma cleaning initially to remove surface contaminants. Photoresist (L300, Seoul, Republic of Korea) was spin-coated on the HfO_2 layer at a speed of 4000 r/min, and the patterned potholes on the HfO_2 layer were achieved through exposure in a photolithography machine. Subsequently, pure vanadium was deposited into the patterned potholes, and the photoresist mask, along with excess vanadium, was eliminated through immersion and ultrasonic delamination in an acetone solution. Following this step, the patterned vanadium microstructure underwent additional thermal treatment to transform the VO_2 (M) phase, thereby producing the final ATMRD.

4.2 Characterization

The morphology was observed by field emission scanning electron microscopy (FE-SEM, Hitachi S-4800, Tokyo, Japan). The phase structure of the films was measured utilizing an XRD (Rigaku SmartLab SE, Tokyo, Japan) and a Raman spectrometer (Horiba LabRAM HR Evolution, Paris, France) equipped with a 532-nm laser. An ultraviolet–visible–near-IR spectrophotometer (UV-VIS-NIR, Agilent UV3600, Santa Clara, California, United States) fitted with an integrating sphere measured the transmittance and reflectivity from 300 to 2500 nm at different temperatures using a homemade heating table. Thermal spectral reflectance was characterized by a Fourier transform IR spectrometer (Nicolet iS50, Madison, Wisconsin, United States) equipped with mid-IR IntegratIR spheres (PIKE Technologies, Inc., Madison, Wisconsin, United States) and mercury cadmium telluride (MCT) detectors over the ~2 to 18 μm wavelength range at 12-deg angle of incidence. According to Kirchhoff's law of radiation, in a state of thermodynamic equilibrium, the spectral emittance $\varepsilon(\lambda, T)$ equals the spectral absorptance $A(\lambda, T)$.[33] As a radiative cooling device comprises a thick Ag layer, the transmittance (T) in the solar and thermal IR wavelength ranges was considered zero. Thus, its thermal spectral emittance in this range was computed as $\varepsilon(\lambda, T) = A(\lambda, T) = 1 - R(\lambda, T)$.

The solar absorptance (α_{sol}) and thermal emittance (ε) can be calculated from the corresponding spectral data using the following equations:

$$\alpha_{sol} = \frac{\int_{0.3\ \mu m}^{2.5\ \mu m} A(\lambda)\phi_{sol}(\lambda)d\lambda}{\int_{0.3\ \mu m}^{2.5\ \mu m} \phi_{sol}(\lambda)d\lambda}, \quad (1)$$

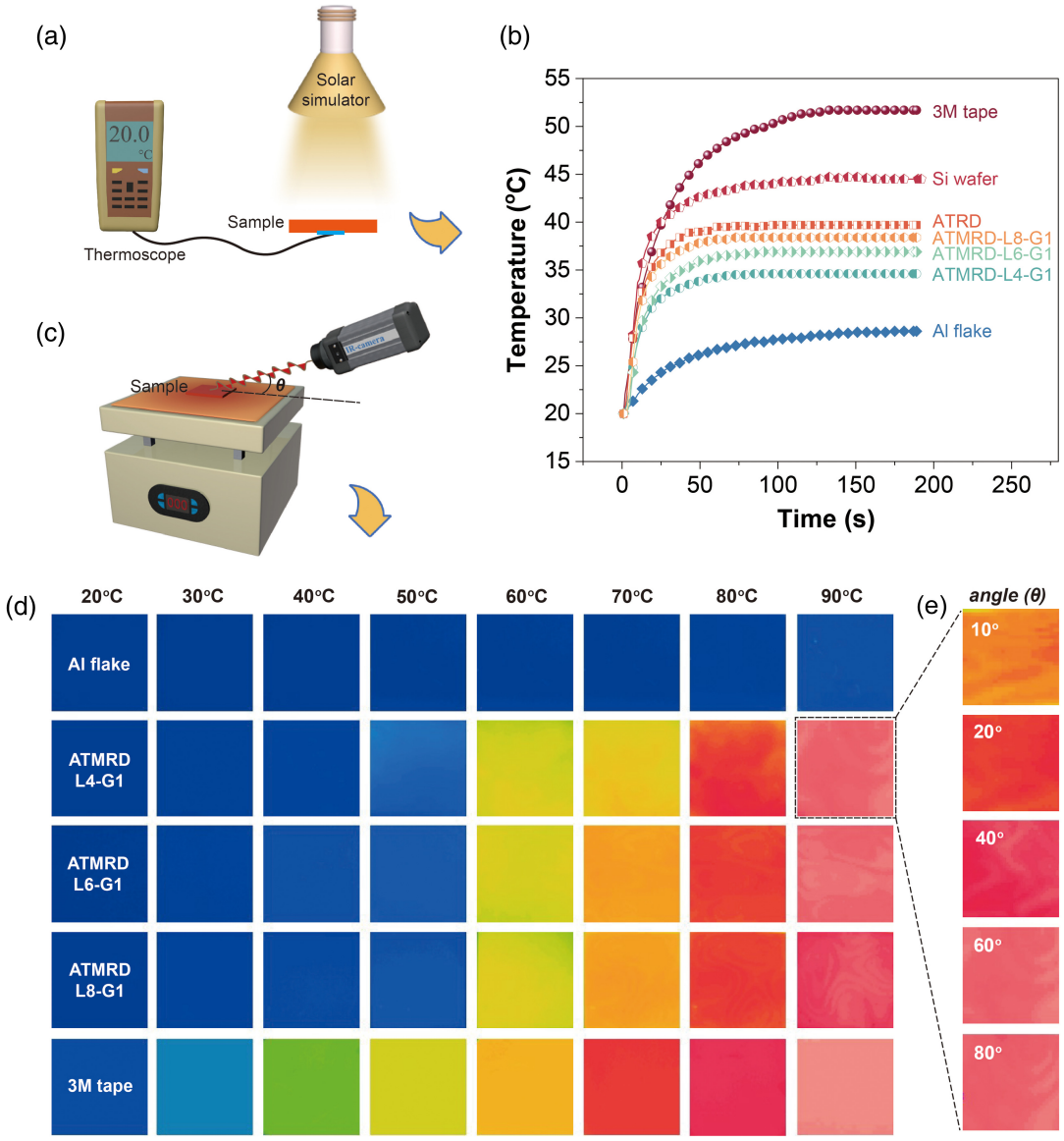

Fig. 8 (a) Schematic of a simulated solar heating test and (c) IR thermal emittance test, and the θ represents different detection angles. (b) Temperature tracking of diverse samples under simulated solar heating. (d) Thermal IR imaging of vertical incidence under different temperatures for Al flake, commercial 3M tape, and different ATMRDs. (e) Thermal IR imaging of the ATMRD L4-G1 at different detection angles at 90°C.

$$\varepsilon(T) = \frac{\int_{8\ \mu\mathrm{m}}^{14\ \mu\mathrm{m}} B(\lambda, T)(1 - R(\lambda, T))\mathrm{d}\lambda}{\int_{8\ \mu\mathrm{m}}^{14\ \mu\mathrm{m}} B(\lambda, T)\mathrm{d}\lambda}, \tag{2}$$

where $A(\lambda)$ is the spectral absorptance at corresponding wavelength λ. $\phi_{\mathrm{sol}}(\lambda)$ is the solar irradiance spectrum for an air mass of 1.5 corresponding to the sun standing 37 deg above the horizon. $R(\lambda, T)$ is the reflectance at wavelength λ and temperature T. $B(\lambda, T)$ is the spectral intensity of blackbody emission at the desired temperature given by Planck's law. By calculating the performance at high and low temperatures, the emittance tunability ($\Delta\varepsilon$) can be obtained: $\Delta\varepsilon = \varepsilon_H - \varepsilon_L$.

The solar heating simulation test was carried out using a solar simulator (PLS-SXE300, Beijing Perfectlight Technology Co., Ltd., Beijing, China), and a temperature recorder fitted with a Pt temperature sensor recorded the temperatures. Before measuring each type of material surface, the shutter of the solar simulator remained closed, and the sample was first stabilized at room temperature. Then, the shutter was opened, and the surface temperature was recorded as a function of time. Thermal IR images were captured by an FLIR A310 infrared camera (IR camera) working at a 7.5- to 14-μm wavelength. To minimize reflections in the surrounding environment, the experiments were conducted in an open, outdoor environment. Before testing, the IR camera was calibrated using a thermocouple and 3M tape (a commercial product with a constant emittance of 0.96) as a reference to ensure that the displayed surface temperature matches the reference sample's actual temperature. The sample was heated using a heating stage, and the IR camera recorded video images at a fixed detection angle.

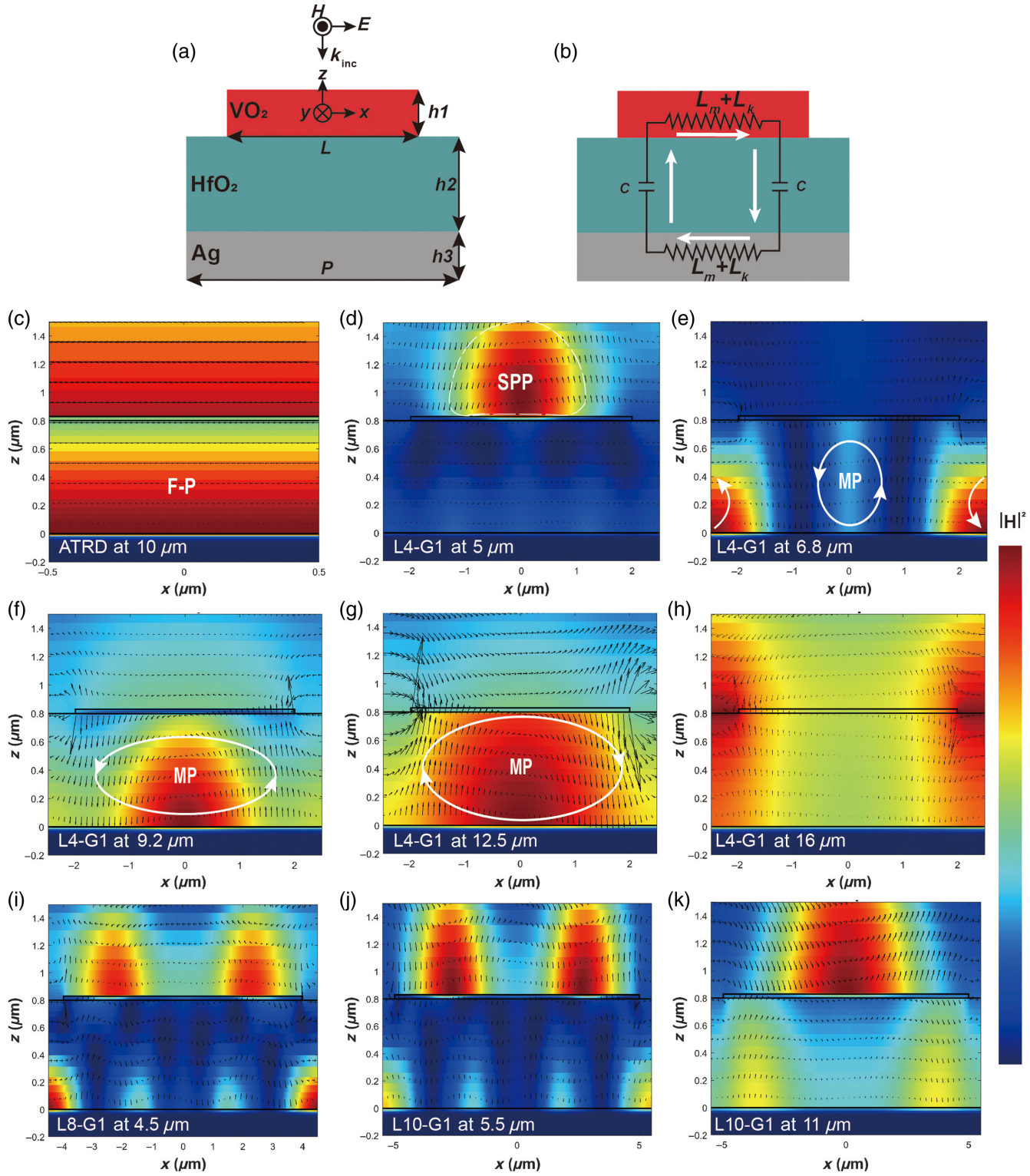

Fig. 9 (a) Schematic diagram of simulated ATMRD using FDTD, the x–z plane at $y = 0$ μm. (b) Equivalent LC circuit model for MP excitation when VO_2 is in the metallic phase. Electromagnetic field distribution of the x–z cross section of one array cell at different wavelengths in the VO_2 metallic phase. (c) ATRD. (d)–(h) ATMRD L4-G1. (i) ATMRD L8-G1. (j), (k) ATMRD L10-G1. Note that the contour color indicates the magnetic field strength, expressed as $|H|^2$, and the black arrows represent the electric field vectors. The white arrow indicates the current loop of the equivalent LC circuit.

4.3 Simulation Design

We used finite-difference time-domain (FDTD, Ansys Lumerical, Canonsburg, Pennsylvania, United States) modeling for numerical simulations of the radiative cooling device. A three-dimensional unit cell model was established, including the VO_2 submicrometer square or circle, HfO_2 layer, and Ag substrate. The materials' optical properties were obtained from Ref. 24 for VO_2 and Ref. 34 for HfO_2. The optical properties of Ag employed in the simulation were calculated from Palik's handbook.[50] The simulation region had a size of $x \times y \times z$ referring to the period of the P micrometer disks. The perfect matching layer boundary conditions were applied along the propagation of electromagnetic waves (z direction), and periodic boundary conditions were applied along the x direction and y direction. A broadband linearly polarized plane wave was directed toward the unit cell from above the structure at normal incidence. Positioned above the plane wave source was a frequency–domain power monitor designed to capture the reflected waves. The simulation exclusively focuses on the transverse magnetic (TM) wave, where metamaterial particles are excited by the y component of the magnetic field. Due to the symmetry of the considered patterns, the reflectance remains consistent for both transverse electric and TM waves. All simulations detailed in this paper are conducted within a three-dimensional computational domain, employing a nonuniform structured mesh with a minimum mesh size of 1 nm.[35]

Disclosures

The authors declare no conflicts of interest.

Code and Data Availability

All the data and methods needed to evaluate the conclusions of this work are presented in the main text and Supplementary Material. Additional data can be requested from the corresponding author.

Author Contributions

J.Y. was associated with conceptualization, investigation, experiments, simulations, formal analysis, writing—original draft and review and editing, methodology, and resources. Q.L., S.L., D.F., and J.Z. were associated with methodology and data curation. H.J. was associated with formal analysis, funding acquisition, writing—review and editing, resources, and project administration supervision. J.L. was associated with conceptualization, formal analysis, writing—review and editing, resources, and project administration supervision. All authors analyzed and discussed the results.

Acknowledgments

This work was supported by the National Natural Science Foundation of China (Grant No. 52371176).

References

1. T. Li et al., "A radiative cooling structural material," *Science* **364**, 760–763 (2019).
2. Y. Peng et al., "Coloured low-emissivity films for building envelopes for year-round energy savings," *Nat. Sustain.* **5**, 339–347 (2021).
3. K. Tang et al., "Temperature-adaptive radiative coating for all-season household thermal regulation," *Science*, **374**, 1504–1509 (2021).
4. S. Wang et al., "Scalable thermochromic smart windows with passive radiative cooling regulation," *Science* **374**, 1501–1504 (2021).
5. X. Ao et al., "Self-adaptive integration of photothermal and radiative cooling for continuous energy harvesting from the sun and outer space," *Proc. Natl. Acad. Sci. U. S. A.* **119**, 2120557119 (2022).
6. K. Lin et al., "Hierarchically structured passive radiative cooling ceramic with high solar reflectivity," *Science* **382**, 691–697 (2023).
7. X. Zhao et al., "A solution-processed radiative cooling glass," *Science* **382**, 684–691 (2023).
8. B. Svetozarevic et al., "Dynamic photovoltaic building envelopes for adaptive energy and comfort management," *Nat. Energy* **4**, 671–682 (2019).
9. J. Yang and X. Hao, "Electrocaloric effect and pyroelectric performance in $(K, Na)NbO_3$-based lead-free ceramics," *J. Am. Ceram. Soc.* **102**, 6817–6826 (2019).
10. J. Yang et al., "Synergistically optimizing electrocaloric effects and temperature span in KNN-based ceramics utilizing a relaxor multiphase boundary," *J. Mater. Chem. C* **8**, 4030–4039 (2020).
11. J. Yang et al., "Enhanced electrocaloric effect of relaxor potassium sodium niobate lead-free ceramic via multilayer structure," *Scr. Mater.* **193**, 97–102 (2021).
12. C. Zhou et al., "Transparent bamboo with high radiative cooling targeting energy savings," *ACS Mater. Lett.* **3**, 883–888 (2021).
13. S. P. Liu et al., "A scalable microstructure photonic coating fabricated by roll-to-roll "defects" for daytime subambient passive radiative cooling," *Nano Lett.* **23**, 7767–7774 (2023).
14. J. Yun et al., "Optimally designed multimaterial microparticle-polymer composite paints for passive daytime radiative cooling," *ACS Photonics* **10**, 2608–2617 (2023).
15. P. Li et al., "Thermo-optically designed scalable photonic films with high thermal conductivity for subambient and above-ambient radiative cooling," *Adv. Funct. Mater.* **32**, 2109542 (2021).
16. B. Zhu et al., "Subambient daytime radiative cooling textile based on nanoprocessed silk," *Nat. Nanotechnol.* **16**, 1342–1348 (2021).
17. X. Wang et al., "Scalable flexible hybrid membranes with photonic structures for daytime radiative cooling," *Adv. Funct. Mater.* **30**, 1907562 (2019).
18. Y. Tian et al., "Surface photon-engineered infrared-black metamaterial enabled enhancement of heat dissipation," *Adv. Funct. Mater.* **32**, 2205016 (2022).
19. D. Zhao and H. Tang, "Staying stably cool in the sunlight," *Science* **382**, 644–645 (2023).
20. Z. Xu et al., "Spatially resolved dynamically reconfigurable multilevel control of thermal emission," *Laser Photonics Rev.* **14**, 1900162 (2019).
21. J. Li et al., "Printable, emissivity-adaptive and albedo-optimized covering for year-round energy saving," *Joule* **7**, 2552–2567 (2023).
22. J. Gu et al., "VO_2-based infrared radiation regulator with excellent dynamic thermal management performance," *ACS Appl. Mater. Interfaces* **14**, 2683–2690 (2022).
23. X. Xu et al., "Passive and dynamic phase-change-based radiative cooling in outdoor weather," *ACS Appl. Mater. Interfaces* **14**, 14313–14320 (2022).
24. R. Beaini et al., "Thermochromic VO_2-based smart radiator devices with ultralow refractive index cavities for increased performance," *Sol. Energ. Mater. Sol. C* **205**, 110260 (2020).
25. L. Liu et al., "Hybrid metamaterials for electrically triggered multifunctional control," *Nat. Commun.* **7**, 13236 (2016).
26. S. Abdollahramezani et al., "Dynamic hybrid metasurfaces," *Nano Lett.* **21**, 1238–1245 (2021).
27. C. Zou et al., "Metal-loaded dielectric resonator metasurfaces for radiative cooling," *Adv. Opt. Mater.* **5**, 1700460 (2017).

28. K. C. S. Ly et al., "A dual-mode infrared asymmetric photonic structure for all-season passive radiative cooling and heating," *Adv. Funct. Mater.* **32**, 2203789 (2022).
29. T. Paik et al., "Solution-processed phase-change VO_2 metamaterials from colloidal vanadium oxide (VO_x) nanocrystals," *ACS Nano* **8**, 797–806 (2014).
30. J. K. Pradhan et al., "High contrast switchability of VO_2-based metamaterial absorbers with ITO ground plane," *Opt. Express* **25**, 9116–9121 (2017).
31. K. Sun et al., "VO_2 thermochromic metamaterial-based smart optical solar reflector," *ACS Photonics* **5**, 2280–2286 (2018).
32. J. Zou et al., "Multiband metamaterial selective absorber for infrared stealth," *Appl. Opt.* **59**, 8768–8772 (2020).
33. J. Agassi, "The Kirchhoff-Planck radiation law," *Science* **156**, 30–37 (1967).
34. T. J. Bright et al., "Optical properties of HfO_2 thin films deposited by magnetron sputtering: from the visible to the far-infrared," *Thin Solid Films* **520**, 6793–6802 (2012).
35. A. Sakurai et al., "Resonant frequency and bandwidth of metamaterial emitters and absorbers predicted by an RLC circuit model," *J. Quant. Spectrosc. Radiat.* **149**, 33–40 (2014).
36. W. Yang et al., "All-dielectric metasurface for high-performance structural color," *Nat. Commun.* **11**, 1864 (2020).
37. J. Yang et al., "Optimizing phase transition temperature and visible transmittance of VO_2 films driven by synergistic effect of La-Mo co-doping," *Appl. Surf. Sci.* **600**, 154074 (2022).
38. A. Hendaoui et al., "Highly tunable-emittance radiator based on semiconductor-metal transition of VO_2 thin films," *Appl. Phys. Lett.* **102**, 061107 (2013).
39. A. Hendaoui et al., "VO_2-based smart coatings with improved emittance-switching properties for an energy-efficient near room-temperature thermal control of spacecrafts," *Sol. Energ. Mater. Sol. C* **117**, 494–498 (2013).
40. X. Wang et al., "Fabrication of VO_2-based multilayer structure with variable emittance," *Appl. Surf. Sci.* **344**, 230–235 (2015).
41. K. Sun et al., "Metasurface optical solar reflectors using AZO transparent conducting oxides for radiative cooling of spacecraft," *ACS Photonics* **5**, 495–501 (2017).
42. H. Kim et al., "VO_2-based switchable radiator for spacecraft thermal control," *Sci. Rep.* **9**, 11329 (2019).
43. S. Taylor et al., "Spectrally-selective vanadium dioxide based tunable metafilm emitter for dynamic radiative cooling," *Sol. Energ. Mater. Sol. C* **217**, 110739 (2020).
44. X. Wu et al., "Passive smart thermal control coatings incorporating CaF_2/VO_2 core-shell microsphere structures," *Nano Lett.* **21**, 3908–3914 (2021).
45. K. Sun et al., "Room temperature phase transition of W-doped VO_2 by atomic layer deposition on 200 mm Si wafers and flexible substrates," *Adv. Opt. Mater.* **10**, 2201326 (2022).
46. M. Liu et al., "Continuous photothermal and radiative cooling energy harvesting by VO_2 smart coatings with switchable broadband infrared emission," *ACS Nano* **17**, 9501–9509 (2023).
47. L. Long et al., "Enhanced infrared emission by thermally switching the excitation of magnetic polariton with scalable microstructured VO_2 metasurfaces," *ACS Photonics* **7**, 2219–2227 (2020).
48. Y. B. Chen and F. C. Chiu, "Trapping mid-infrared rays in a lossy film with the Berreman mode, epsilon near zero mode, and magnetic polaritons," *Opt. Express* **21**, 20771–20785 (2013).
49. B. Zhao and Z. M. Zhang, "Study of magnetic polaritons in deep gratings for thermal emission control," *J. Quantum Spectrosc. Radiat.* **135**, 81–89 (2014).
50. E. D. Palik, *Handbook of Optical Constants of Solids*, Vol. **3**, Academic Press (1998).

Junlin Yang is a PhD candidate at the Beijing Institute of Technology, under the supervision of professor Jingbo Li. His research primarily focuses on the structure and performance regulation of thermochromic phase change materials and the design of radiative thermal control devices.

Haibo Jin is a professor at the Beijing Institute of Technology. His main research interests focus on functional materials and energy storage and conversion, with a primary emphasis on key materials and technologies for secondary batteries and hydrogen energy development. He has published over 100 papers, which have been cited more than 10,000 times, and holds 15 authorized invention patents. He was once selected as one of the "top 1% highly cited Chinese authors" by a journal of the Royal Society of Chemistry.

Jingbo Li is a professor at the Beijing Institute of Technology. His research focuses on novel electromagnetic functional materials, multi-field regulation, and device design and fabrication, with a primary emphasis on key materials and technologies for broadband intelligent electromagnetic modulation and the development of energy-saving windows. He has led and completed more than 10 major projects, published over 100 papers, held 12 national invention patents, and edited 2 textbooks.

Biographies of the other authors are not available.